







Cite as
Nano-Micro Lett.
(2021) 13:60

Received: 7 October 2020
Accepted: 8 December 2020
Published online: 21 January 2021
© The Author(s) 2021

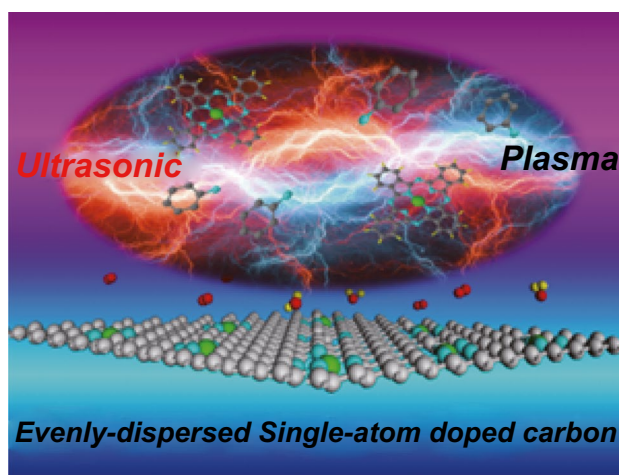
Ultrasonic Plasma Engineering Toward Facile Synthesis of Single-Atom M-N₄/N-Doped Carbon (M = Fe, Co) as Superior Oxygen Electrocatalyst in Rechargeable Zinc–Air Batteries

Kai Chen¹, Seonghee Kim¹, Minyeong Je², Heechae Choi²  , Zhicong Shi³, Nikola Vladimirov⁴, Kwang Ho Kim^{1,5} , Oi Lun Li¹ 

HIGHLIGHTS

- Single-atom M-N₄/N-doped carbons (M = Fe, Co) prepared as OER/ORR catalysts.
- Ultrasonication-assisted plasma engineering used for catalyst synthesis.
- Co-N₄/NC outperformed benchmark commercial catalysts in practical Zn–air battery test.
- DFT calculations provided insights into the origin of superior ORR/OER performance.

ABSTRACT As bifunctional oxygen evolution/reduction electrocatalysts, transition-metal-based single-atom-doped nitrogen–carbon (NC) matrices are promising successors of the corresponding noble-metal-based catalysts, offering the advantages of ultrahigh atom utilization efficiency and surface active energy. However, the fabrication of such matrices (e.g., well-dispersed single-atom-doped M-N₄/NCs) often requires numerous steps and tedious processes. Herein, ultrasonic plasma engineering allows direct carbonization in a precursor solution containing metal phthalocyanine and aniline. When combining with the dispersion effect of ultrasonic waves, we successfully fabricated uniform single-atom M-N₄ (M = Fe, Co) carbon catalysts with a production rate as high as 10 mg min⁻¹. The Co-N₄/NC presented a bifunctional potential drop of $\Delta E = 0.79$ V, outperforming the benchmark Pt/C–Ru/C catalyst ($\Delta E = 0.88$ V) at the same catalyst



Kai Chen and Minyeong Je contributed equally and should be regarded as co-first authors.

✉ Heechae Choi, h.choi@uni-koeln.de; Kwang Ho Kim, kwhokim@pusan.ac.kr; Oi Lun Li, helenali@pusan.ac.kr

¹ Department of Materials Science and Engineering, Pusan National University, 30 Jangjeon-dong, Geumjeong-gu, Busan 609-735, Republic of Korea

² Theoretical Materials and Chemistry Group, Institute of Inorganic Chemistry, University of Cologne, Greinstr. 6, 50939 Cologne, Germany

³ School of Materials and Energy, Guangdong University of Technology, Guangzhou 510006, People's Republic of China

⁴ Faculty of Mechanical Engineering and Naval Architecture, University of Zagreb, Ivana Lucica 5, 10002 Zagreb, Croatia

⁵ Global Frontier R&D Center for Hybrid Interface Materials, 30 Jangjeon-dong, Geumjeong-gu, Busan 46241, Republic of Korea



loading. Theoretical calculations revealed that Co-N₄ was the major active site with superior O₂ adsorption–desorption mechanisms. In a practical Zn–air battery test, the air electrode coated with Co-N₄/NC exhibited a specific capacity (762.8 mAh g⁻¹) and power density (101.62 mW cm⁻²), exceeding those of Pt/C–Ru/C (700.8 mAh g⁻¹ and 89.16 mW cm⁻², respectively) at the same catalyst loading. Moreover, for Co-N₄/NC, the potential difference increased from 1.16 to 1.47 V after 100 charge–discharge cycles. The proposed innovative and scalable strategy was concluded to be well suited for the fabrication of single-atom-doped carbons as promising bifunctional oxygen evolution/reduction electrocatalysts for metal–air batteries.

KEYWORDS Single-atom-doped M-N₄/NC catalyst; Plasma engineering; ORR/OER bifunctional activity; DFT calculation; Rechargeable Zn–air battery

Abbreviations

NC	Nitrogen-doped carbon
DFT	Density functional theory
ORR	Oxygen reduction reaction
OER	Oxygen evolution reaction
ZAB	Zinc–air battery
MOF	Metal–organic framework
XRD	X-ray diffraction
FE-STEM	Field-emission scanning transmission electron microscopy
EELS	Electron energy loss spectroscopy
XPS	X-ray photoelectron spectroscopy
EXAFS	X-ray absorption fine structure
XANES	X-ray absorption near-edge structure
RHE	Reversible hydrogen electrode
LSV	Linear sweep voltammetry
CA	Chronoamperometry
CV	Cyclic voltammetry
TEM	Transmission electron microscopy
SAED	Selected area electron diffraction
HR-TEM	High-resolution transmission electron microscopy
HAADF-STEM	High-angle annular dark-field scanning transmission electron microscopy

1 Introduction

The growing demand for green and renewable energy has inspired the vigorous development of power conversion and storage devices (e.g., fuel cells as well as metal–air and secondary batteries) that reveal high power densities and are cheap, safe to handle, and eco-friendly [1–5]. Among the numerous energy conversion devices, rechargeable zinc–air batteries (ZABs) feature a decent theoretical density (1084 Wh kg⁻¹) and high safety; thus, they are potentially suited for application in electric vehicles and portable electronic devices [5, 6]. However, the widespread commercialization of these batteries is hindered by their large

overpotentials for the oxygen reduction reaction (ORR) and the oxygen evolution reaction (OER) [7]. Given that noble-metal-based ORR/OER electrocatalysts (such as Pt and Ru/Ir) suffer from high cost and poor stability during repeated charge–discharge [8], it is essential to develop new bifunctional ORR/OER catalysts with high activity and cycling stability and containing earth-abundant elements as replacements of noble-metal-based catalysts in rechargeable ZABs [9].

Transition-metal-based single-atom-doped nitrogen–carbon electrocatalysts (M-N₄/NCs) are promising successors of noble-metal-based nanocatalysts, exhibiting excellent ORR/OER activity due to their ultrahigh atom utilization efficiency and surface active energy [1]. The superior catalytic activity of M-N₄/NCs mainly originates from the specific coordination between transition metal atoms and nitrogen, which provides a highly efficient means of modifying local electronic states [10, 11]. For instance, Han et al. [1] presented a single-atom Fe–N_x–C ORR electrocatalyst with a high positive half-wave potential and open-circuit voltage, while Zhu et al. [12] prepared hierarchically porous M–N_x–C (M = Co, Fe) single-atom electrocatalysts with superior ORR activity as a result of the rise active sites. Thus, the introduction of transition metals as monoatom active sites into N-doped carbon (NC) matrices is a suitable way of improving ZAB performance. Despite these achievements, the fabrication of well-dispersed M-N₄/NCs remains challenging. Notably, control of the interfacial contact between the metal atoms and the charcoal support as well as that of metal atom dispersion are crucial for ORR/OER activity enhancement. The currently known M-N₄/NC catalysts are largely synthesized by pyrolysis of transition-metal-based metal–organic frameworks (MOFs) [13–17] and metal phthalocyanines [18, 19] or by the chemical polymerization of metal-salt-impregnated organic precursors, such as urea, melamine, or aniline, followed by pyrolysis with a conductive carbon

matrix at 700–1000 °C [20–24]. Moreover, rigid structures like zeolite imidazole frameworks [25, 26] or functionalized carbons with oxygenated groups should be used as supports to immobilize metal ions and thus prevent the aggregation of metal species during thermal treatment [27]. Although these methods allow one to obtain carbon matrices with various atomically dispersed metal centers, they require numerous steps and tedious processes to synthesize appropriate precursors, and the corresponding carbonization ratios and production rates remain low [28]. In addition, the decrease in particle size to the single-atom level often increases surface free energy and thus facilitates the aggregation of metal active sites to form larger clusters or nanoparticles at high pyrolysis temperatures. Consequently, one should establish a facile and scalable strategy of incorporating single metal atoms during carbon synthesis and aim to reduce the temperature of thermal treatment to prevent the aggregation of these atoms into clusters.

Unlike conventional syntheses of single-metal-atom-doped carbon, which require high annealing temperatures for complete carbonization, plasma engineering allows direct carbonization in a precursor solution in an organic solvent (e.g., benzene) [29] or in a solution containing nitrogen and carbon (e.g., pyridine, phenylamine) [30, 31] at ambient temperature and pressure. Specifically, the generation of NC can be achieved via rapid C–N and/or C–C integration during plasma discharge and the related chemical reactions [31]. For instance, B–N double-site-doped carbon was prepared by supplementing the precursors with boric acid and/or phenylboronic acid [31, 32]. The mechanisms of the in situ syntheses of heteroatom-doped carbons via plasma engineering have been thoroughly reviewed by Li et al. [33]. More importantly, Morishita et al. reported that the rate of carbon production from benzene derivatives (e.g., benzene and aniline) via plasma synthesis ($1\text{--}10\text{ mg min}^{-1}$) substantially exceeds that of pyrolytic methods [34]. Thus, it was hypothesized that plasma engineering can be used to effectively prepare single-atom-doped catalysts from aniline and metal phthalocyanines. During plasma engineering, direct carbonization proceeds by the combination of CN and C₂ radicals with the solution precursor at the gas/liquid interface. Since the metal phthalocyanine has high chemical stability and is only present in small amount in the solution phase, the molecular structure is expected to maintain its planar metal-N₄ coordination during the fast formation of carbon materials. Also, the solubility of metal

phthalocyanines is very low in pure aniline, which might result in easy agglomeration. An ultrasonic homogenizer uses the dispersion effect of ultrasonic waves in the liquid to cause cavitation of the liquid, which is useful in mixing, emulsifying, dispersing, and deagglomeration [35]. To the best of our knowledge, this is the first study to combine plasma engineering with ultrasonication-assisted homogenization to prevent agglomeration during the synthesis and to successfully dope molecular M-N₄ atomically within the NC matrix with a high production rate of $\sim 10\text{ mg min}^{-1}$.

Among the screened metal phthalocyanines, M-N₄ structures featuring Fe and Co as central metal atoms exhibited the best ORR/OER catalytic activity in an alkaline electrolyte [36]. Wang et al. [37] applied iron phthalocyanine (Fe-Pc) as an analog to FeN₄ and explored the ORR activity by means of comprehensive density functional theory (DFT) computations. It was found that O₂ could readily bind to the Fe center with charge transfer from Fe to O₂, and O₂* reduction was identified as the rate-determining step. Moreover, Peng et al. [38] indicated that the number of states around the Fermi level was significantly higher for the FeN₄ moiety with dominant contributions from the Fe 3d orbital based on DFT density of states plots. This indicates that the Fe center is favorable for the adsorption of O₂ and may donate electrons to reduce O₂, which results in superior ORR catalytic activity. In contrast, the contribution of Co-N₄ seems to be more significant in OER process. Fei et al. investigated the MN₄C₄ (M = Fe, Co, and Ni) moieties in a graphene matrix by DFT calculations and experimental studies [39]. In the theoretical calculations, the free energy of the rate-determining step (RDS) for Fe–NHGF is the oxidation of O* to OOH* with limiting barrier energy as large as 0.97 eV. In the case of Co–NHGF, the RDS is the oxidation of OH* to O* with much lower limiting barrier of 0.52 eV. The experimental results also agreed with the DFT calculation and supported the advanced OER catalytic activity in Co moieties.

Herein, single-atom Fe-N₄/NC and Co-N₄/NC catalysts were prepared via ultrasonication-assisted plasma engineering. High-purity aniline was used as a solvent and NC matrix precursor, while the metal phthalocyanine (M = Fe, Co) acted as a coupling agent and precursor to form the M-N₄ matrix. As the thermal decomposition of these phthalocyanines normally occurs at 570–750 °C [40], a mild annealing temperature of 550 °C was chosen for the single-atom catalyst synthesis to enhance the graphitization of NC and preserve the M-N₄ molecular structure. The very low

solubility of metal phthalocyanines in pure aniline results in easy agglomeration under typical plasma synthesis conditions, if there are no external forces to keep these large molecules separated. Thus, an ultrasonic homogenizer was additionally employed to ensure the atomic-level dispersion of M-N₄ within the nitrogen–carbon matrix during plasma engineering. To verify the importance of homogenization, Co-N₄/NC was synthesized in the absence of the above homogenizer under otherwise identical conditions, and Co nanoparticles were detected in the resulting NC matrix (Fig. S1a–e). The corresponding X-ray diffraction (XRD) pattern featured peaks at $2\theta = 44^\circ$, 52° , and 76° that were ascribed to the [110], [200], and [220] planes of Co metal, respectively (Fig. S1f). Notably, our novel strategy allowed the facile synthesis of atomically dispersed M-N₄/NC (M = Fe, Co) electrocatalysts with ORR/OER activities and stabilities superior to those of commercial noble-metal-based catalysts. Specifically, Co-N₄/NC exhibited a bifunctional potential drop ($\Delta E = E_{j=10} - E_{1/2} = 0.79$ V) superior to that of the benchmark Pt/C-Ru/C ($\Delta E_{\text{Pt/C-Ru/C}} = 0.88$ V) at the same loading. Free energy changes determined by density functional theory (DFT) calculations suggested that the O₂ adsorption–desorption performance of Co-N₄/NC is superior to that of the well-studied Fe-N₄/NC, in line with experimental results. Finally, in rechargeable ZABs, the Co-N₄/NC-based air electrode achieved higher power density, higher specific capability, and better durability than that constructed using a commercial Pt/C-Ru/C catalyst.

2 Experimental

2.1 Synthesis of M-N₄/N-Doped Carbons

The metal (Fe, Co) phthalocyanine (~95%, Sigma-Aldrich, Korea) was dissolved in aniline (100 mL; >99%, Junsei Chemical Co., Ltd., Japan) for 1 h upon magnetic stirring to achieve a concentration of 1 mM. Then, two high-purity graphite electrodes were discharged in this solution at a voltage of 1.2 kV, a frequency of 25 kHz, and a pulse width of 0.9 μs for 20 min (Pulse Modulator, MPP04-A4-200, Japan), with the assistance of an ultrasonic homogenizer (Korea Process Technology Co., Ltd., KSC-80, 25 kHz) [31]. The liquid phase was passed through a 55-mm-diameter polytetrafluoroethylene filter and evaporated at 80 °C for 10 h. The resulting product was heated at 550 °C for 2 h

in N₂ to enhance conductance and denoted as Fe-N₄/NC and Co-N₄/NC.

2.2 Electrocatalyst Characterization

Morphologies and elemental distributions were probed by field-emission scanning transmission electron microscopy (FE-STEM; HD-2300A, Hitachi, Japan) at an operating voltage of 200 kV. Individual elements were identified by electron energy loss spectroscopy (EELS; JEM-ARM200F, JEOL, Japan). Crystalline phases were identified by XRD analysis (Ultima IV, Rigaku, Japan). Nanocomposite graphitization degree, irregularities, and imperfections were characterized by Raman spectroscopy (VERTEX 80v, Bruker, Korea). Surface chemical states were identified by X-ray photoelectron spectroscopy (XPS; Kratos Analytical Ltd., Axis Supra, UK). The absolute metal contents of carbon catalysts were probed by inductively coupled plasma optical emission spectrometry (Optima 8300, Perkin Elmer, USA). Fe K-edge- and Co K-edge-extended X-ray absorption fine structure (EXAFS) spectra were recorded according to fluorescent patterns using the TPS 44A1 beamline (situated in the National Synchrotron Radiation Research Center (NSRRC) of Taiwan, China) at an energy of 3 GeV and an average current of 250 mA [41]. The radioactive ray was monochromatized by a monochromator with Si (111) bicrystal. X-ray absorption near-edge structure (XANES) and EXAFS data reduction and analysis were performed using Athena software [41].

2.3 Electrochemical Measurements

The electrochemical characteristics of ORR/OER catalysts were investigated using a benchmark three-electrode system and an electrochemical workstation (Biologic, VSP, France) [31]. All measurements were conducted in 0.1 M KOH (specification of analysis, Samchun Co., Ltd.) solution at ambient temperature and pressure. Typically, M-N₄/NC (4 mg) was dispersed into the solution of deionized water (480 μL), ethanol (480 μL , 99.9%, Duksan Co., Ltd.), and Nafion[®]117 (40 μL , 5 wt %, Aldrich Co., Ltd.) by 30-min ultrasonication to produce a well-distributed catalyst ink. The ink was drop-cast onto a well-polished glassy carbon disk electrode ($R_{\text{diameter}} = 4$ mm) and dried under ambient conditions to afford a loading of 800 $\mu\text{g}/$

cm². A Pt wire was used as a counter electrode, while Hg/HgO in 1 M NaOH was regarded as a reference electrode. Every electric potential was calibrated using the reversible hydrogen electrode (RHE) conversion formula, $E_{\text{RHE}}(\text{V}) = E_{\text{Hg/HgO(1MNaOH)}} + 0.198 + 0.059\text{pH}$. For ORR analysis, polarization curves were constructed using linear sweep voltammetry (LSV) measurements in O₂-saturated 0.1 M KOH at a scanning speed (5 mV s⁻¹) and a rotation rate (1600 rpm) within a voltage region (0.2–1.2 V vs. RHE). Chronoamperometry (CA) measurement of Co-N₄/NC was performed at 0.6 V versus RHE for 30,000 s to examine cycling stability and catalyst durability. Also, chronopotentiometry (CP) response at a certain current density (−4 mA cm⁻²) for the Co-N₄/NC was measured to verify the durability and stability. Cyclic voltammetry (CV) measurements were carried out at 100 mV s⁻¹ in the voltage range 0.4–1.0 V versus RHE for 3000 cycles. Additionally, the average electron transfer number (*n*) and the yield of H₂O₂ were measured based on rotating ring–disk electrodes (RRDE) analysis. It is expressed by the following equation:

$$n = 4 \times I_d / (I_d + I_r/N) \quad (1)$$

$$\text{H}_2\text{O}_2 (\%) = 200 \times I_r \times N^{-1} / (I_d + I_r/N) \quad (2)$$

where *I_d*, *I_r*, and *N* denote the disk current, ring current, and current collection efficiency, respectively.

For OER analysis, LSV measurements were conducted in O₂-saturated 0.1 M KOH at a scan rate of 5 mV s⁻¹ and a rotation rate of 1600 rpm within the potential range 1–1.8 V versus RHE. CA measurements were performed at 1.6 V versus RHE for 5000 s to investigate catalyst cycling stability, while CV measurements were performed at 100 mV s⁻¹ for 3000 cycles in the potential range 1–1.6 V versus RHE. Electrochemical impedance spectra were recorded in a frequency range from 100 kHz to 100 mHz at 0.9 V versus RHE. For comparison, 20 wt % Pt/C (product code: 591278-1, Fuel Cell Store, USA) and 5 wt % Ru/C (product code: 1002653245, Aldrich Co., Ltd. USA) were used as benchmark ORR and OER catalysts, respectively.

2.4 DFT Calculations

DFT calculations were performed using the Vienna ab initio software package [42, 43]. Interactions between valence and

core electrons were modeled using the projector-augmented wave method [44]. The plane-basis wave expansion was analyzed using the generalized gradient approximation with the Perdew–Burke–Ernzerhof functional [45]. The cutoff energy was 400 eV. The Brillouin area was divided by the sampled grids of 2 × 2 × 1 gamma-centered *k*-points in both vertical and lateral graphene supercells with embedded M-N₄ (M = Fe, Co) structures [46]. A smearing width of 0.1 eV was used in the Methfessel–Paxton smearing scheme [42]. In the self-consistent calculation, the energy convergence domain was set to 10⁻⁵ eV, and the geometric configuration was completely relaxed until Hellman–Feynman forces reached 0.02 eV Å⁻¹. The binding energies of OH, O, OOH, and O₂ were calculated to determine the OER- and ORR-induced energy changes of M-N₄ (M = Fe, Co). The Gibbs free energy (ΔG) change of the response was calculated as:

$$\Delta G = \Delta E + \Delta \text{ZPE} - T\Delta S + \Delta G_U + 0.059 \text{pH} \quad (3)$$

where ΔE is the calculated total energy difference, and ΔZPE , $T\Delta S$, and ΔG_U are the zero-point energy correction, entropy contribution, and free energy term related to the applied electrode potential *U*, respectively.

2.5 Rechargeable ZAB Testing

Testing was performed with the as-prepared electrocatalysts loaded on the gas diffusion layer of the air electrode of an in-house-made ZAB at room temperature. The catalyst ink was prepared as described above and drop-cast onto carbon paper at a mass loading of 1 mg cm⁻². The air cathode was coated with a 1:1 (w/w) mixture of 20 wt % Pt/C and 5 wt % Ru/C at the same total catalyst loading. Zn foil was used as the metal anode, and a solution containing 6 M KOH (Guaranteed Reagent, Junsei Co., Ltd.) and 0.2 M zinc acetate (Sigma-Aldrich Co., Ltd.) was used as the electrolyte. Polarization curves were constructed by performing LSV measurements at a sweep rate of 10 mV s⁻¹ using an electrochemical workstation (Biologic, VSP, France). Specific capacity and energy density were calculated as [47]

$$\text{Energy density (mW cm}^{-2}\text{)} = IV\Delta t / \omega_{\text{Zn}} \quad (4)$$

$$\text{Specific capacity (mA h g}^{-1}\text{)} = I\Delta t / \omega_{\text{Zn}} \quad (5)$$

where *I*, *V*, Δt , and ω_{Zn} represent the current, average discharge voltage, testing time, and amount of consumed Zn, respectively.

Galvanostatic charge–discharge behavior was characterized using the same system. In the cycling test, 100 charge–discharge (5 min + 5 min) cycles were performed at a current density of 10 mA cm^{-2} .

3 Results and Discussion

3.1 Catalyst Fabrication and Characterization

Figure 1 presents the synthesis of $M\text{-N}_4/\text{NC}$ ($M = \text{Fe, Co}$) electrocatalysts via ultrasonication-assisted plasma engineering. The prepared $M\text{-N}_4/\text{NC}$ s were converted into isolated single-atom $M\text{-N}_4/\text{NC}$ s by 2-h annealing in N_2 at 550°C . In addition, NC was synthesized from pure aniline as a control. The production rates of $M\text{-N}_4/\text{NC}$ and NC were close to 10 mg min^{-1} , which agreed with values reported for similar processes [33, 34]. Transmission electron microscopy (TEM) imaging and elemental mappings (Fig. 2a–d and h–k, respectively) showed that $\text{Co-N}_4/\text{NC}$ and $\text{Fe-N}_4/\text{NC}$ contained the respective metal, N, and C. The selected area electron diffraction (SAED) patterns (insets in Fig. 2a, h) had ringlike features indicative of poor crystallinity and the absence of metal nanocrystals. High-resolution transmission electron microscopy (HR-TEM) bright-field imaging demonstrated the presence of several graphitic carbon layers with a lattice spacing of $\sim 0.34 \text{ nm}$ directed toward the (002) plane of $\text{Co-N}_4/\text{NC}$ and $\text{Fe-N}_4/\text{NC}$ (Fig. 2e, o, respectively). Aberration-corrected high-angle annular dark-field scanning transmission electron microscopy (HAADF-STEM) images of $\text{Co-N}_4/\text{NC}$ and $\text{Fe-N}_4/\text{NC}$ revealed the presence of isolated

single-atom Co and Fe sites (Fig. 2f, p, respectively). The atomic-level distributions of Co and Fe were further characterized by EELS. When the electron beam was directed at various positions (yellow regions in Fig. 2f and red regions in Fig. 2p), the obtained EELS spectra showed distinct small peaks of atomic Co and Fe (Fig. 2g, q, respectively). The metal contents of $\text{Co-N}_4/\text{NC}$ and $\text{Fe-N}_4/\text{NC}$ were determined by inductively coupled plasma atomic emission spectrometry as 0.26 and 0.29 wt %, respectively. The above findings support the successful fabrication of dispersed single-atom $\text{Co-N}_4/\text{NC}$ and $\text{Fe-N}_4/\text{NC}$ electrocatalysts.

The XRD patterns of as-prepared $M\text{-N}_4/\text{NC}$ s and pristine NC (Fig. S3) featured similar broad peaks at 23° and 43° , which were indexed to the (002) and (101) planes of graphitic carbon, respectively. Notably, no peaks attributable to crystalline metal nanoparticles were detected. Furthermore, the peak of the (002) plane of graphitic carbon in $M\text{-N}_4/\text{NC}$ s was slightly shifted to the right compared to that of NC, which indicated that the introduction of single-atom $M\text{-N}_4$ units increased the average size of defects in the carbon matrix. The Raman spectra of $M\text{-N}_4/\text{NC}$ s and NC (Fig. S4) featured two major characteristic peaks, viz. the D-band (1344 cm^{-1}) and the G-band (1587 cm^{-1}), with the I_D/I_G intensity ratios of $\text{Co-N}_4/\text{NC}$ and $\text{Fe-N}_4/\text{NC}$ determined to be 1.00 and 1.01, respectively. In contrast, a smaller value of 0.91 was obtained for NC. As the incorporation of single-atom $M\text{-N}_4$ units created larger defects within the NC matrix, it is reasonable that $\text{Co-N}_4/\text{NC}$ and $\text{Fe-N}_4/\text{NC}$ presented a higher I_D/I_G ratio than NC. The N_2 adsorption–desorption isotherms of $M\text{-N}_4/\text{NC}$ s and NC (Fig. S5) could be classified as type IV, indicating

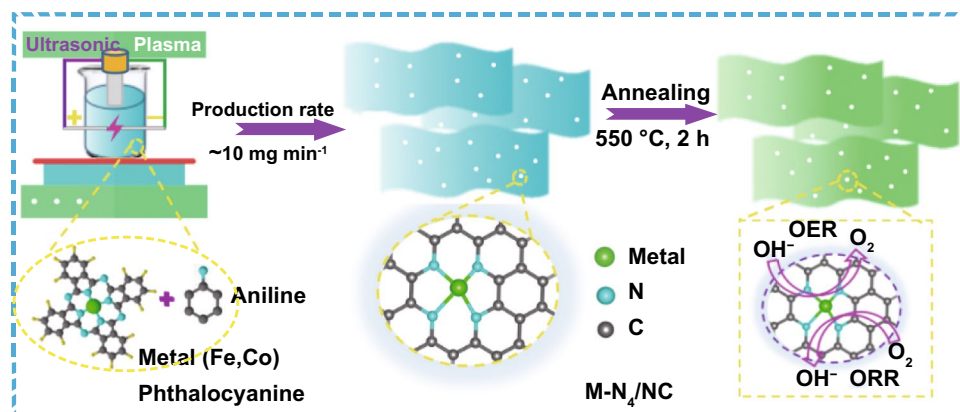


Fig. 1 Schematic of ultrasonic plasma engineering fabrication of $M\text{-N}_4/\text{NC}$ ($M = \text{Fe, Co}$)

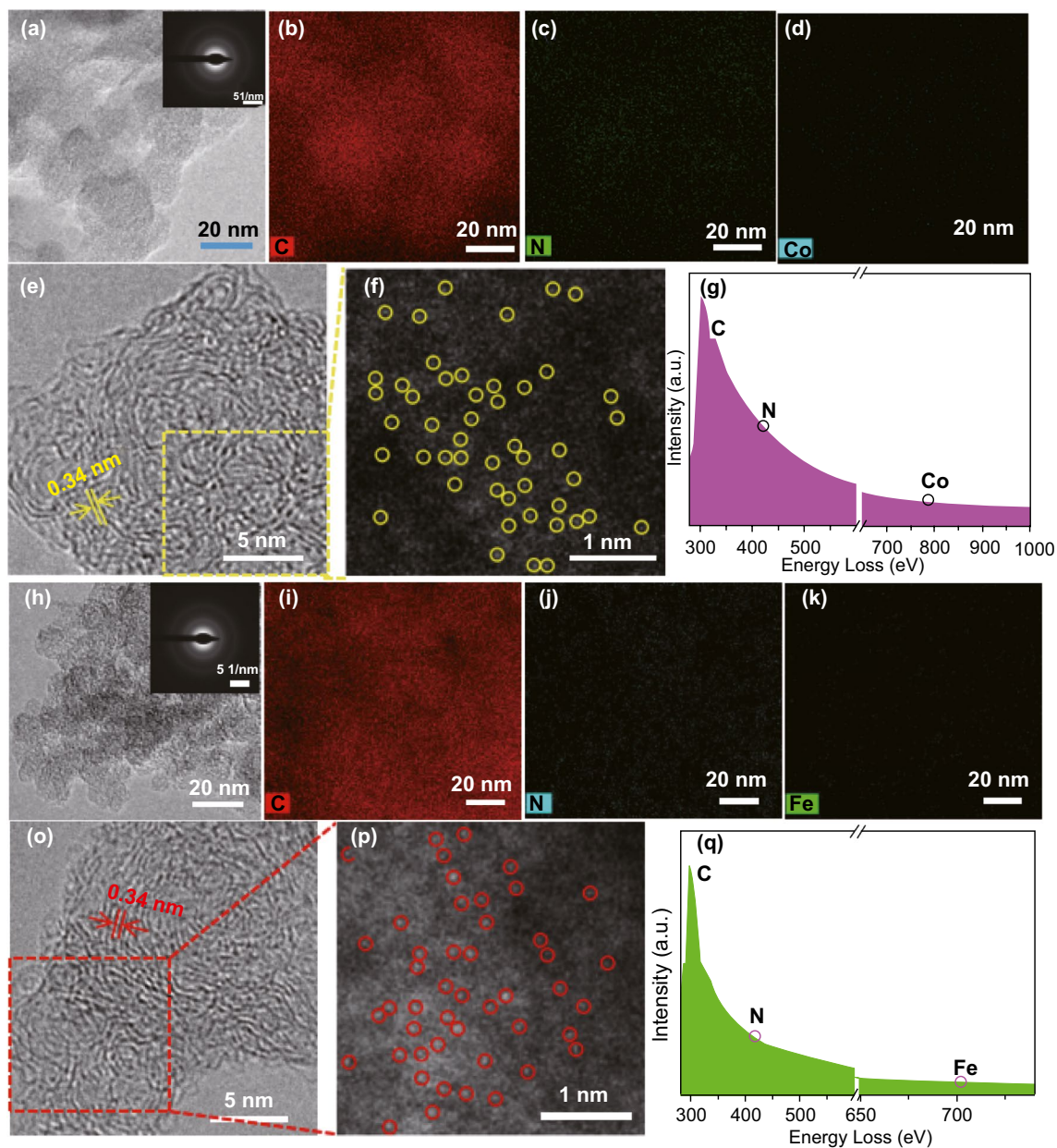


Fig. 2 **a–d** TEM image of Co-N₄/NC (inset: SAED pattern) and elemental mapping of Co, N, and C. **e** HR-TEM (bright field). **f** Aberration-corrected HAADF-TEM image. Enlarged pattern of Co-N₄/NC and partial single Co atoms (yellow). **g** EELS atomic spectra of Co, N, and C elements corresponding to **f**. **h–k** TEM image of Fe-N₄/NC (inset: SAED pattern) and elemental mapping of Fe, N, and C. **l** HR-TEM (bright field). **m** Aberration-corrected HAADF-TEM image of Fe-N₄/NC and partial single Fe atoms (red). **n** EELS atomic spectra of Fe, N, and C elements corresponding to **m**

a mesoporous structure. Moreover, the narrow hysteresis loop in the region of $p/p_0 > 0.9$ suggested the existence of larger mesopores ascribed to the interior of graphene nanospheres. The Brunauer–Emmett–Teller surface areas of Co-N₄/NC and Fe-N₄/NC were estimated as 257.91 and 275.68 m² g⁻¹, respectively (Fig. S6 and Table S2). The

relatively large surface area of M-N₄/NCs can dramatically diminish the proton spread path and accelerate ion diffusion between the electrode and the electrolyte [48]. Combined with morphological and structural analyses, plasma engineering offers a facile route to NC matrices containing well-dispersed single metal atoms.

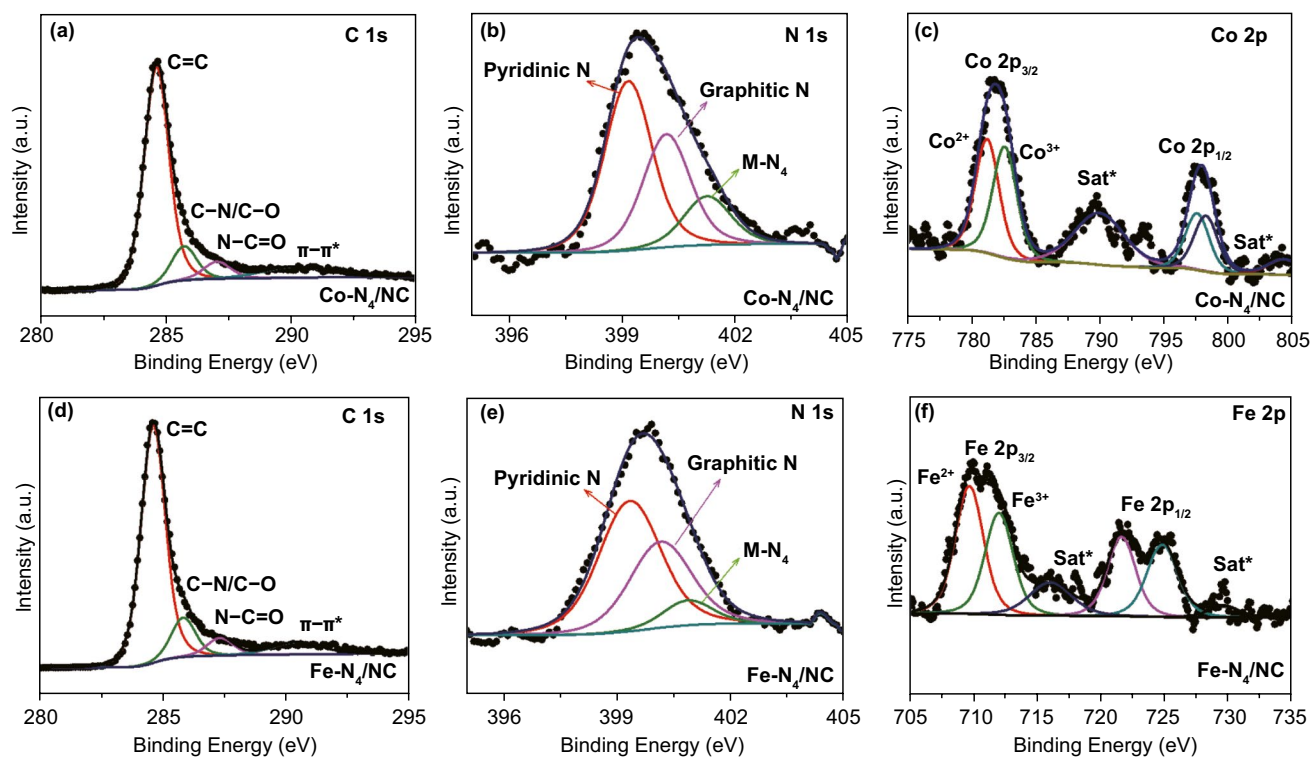


Fig. 3 XPS narrow scan of **a** C 1s, **b** N 1s, and **c** Co 2p for Co-N₄/NC. XPS narrow scan of **d** C 1s, **e** N 1s, and **f** Fe 2p for Fe-N₄/NC

Survey X-ray photoelectron spectra (Fig. S7) indicated the coexistence of metals (Fe, Co) and N in the graphitic carbon networks of Co-N₄/NC and Fe-N₄/NC. Figure 3 provides further insights into the chemical states of each element, presenting the C, N, and Co/Fe narrow-scan spectra of M-N₄/NCs. The high-resolution C 1s spectra of Co-N₄/NC and Fe-N₄/NC (Fig. 3a, d, respectively) featured three main peaks attributed to sp^2 C=C (284.6 eV), C-N/C-O (285.1 eV), and N-C=O (286.8 eV). The high-resolution N 1s spectra of Co-N₄/NC and Fe-N₄/NC (Fig. 3b, e, respectively) showed three major peaks at 398.7, 400.5, and 401.0 eV, which corresponded to pyridinic, graphitic, and metal-bound nitrogen, respectively. In particular, the sharp peak of metal-bound nitrogen confirmed the existence of single-atom active sites, which are expected to contribute to enhanced ORR and OER activities [49]. The high-resolution Co 2p spectrum of Co-N₄/NC (Fig. 3c) showed spin-orbit doublets at 781.6 eV (Co 2p_{3/2}) and 796.3 eV (2p_{1/2}), as well as two satellite peaks at 788.4 and 802.5 eV. The peak spacing of 14.7 eV between the two peaks of Co 2p_{3/2} and Co 2p_{1/2} indicated the presence of both Co²⁺ and Co³⁺ [50]. Based on the fitting of the Co 2p_{3/2} peak, the surface

atomic ratio of Co²⁺/Co³⁺ was calculated as 1.54. Similarly, the high-resolution Fe 2p spectrum (Fig. 3d) featured two spin-orbit doublets at 711.3 eV (Fe 2p_{3/2}, split into two small peaks of Fe²⁺ and Fe³⁺) and 722.8 eV (Fe 2p_{1/2}). The Fe²⁺/Fe³⁺ surface atomic ratio was calculated as 1.26 from the results of Fe 2p_{3/2} peak fitting. The above findings confirmed the presence of M-N bonds in M-N₄/NCs [51].

The metal valence states and chemical environments of M-N₄/NCs were further probed at the atomic level by XANES and EXAFS spectroscopy. Figure 4a presents the Co K-edge XANES spectrum of Co-N₄/NC and those of Co foil, CoO, Co₃O₄, and CoPc as four control references. Co-N₄/NC presented a pre-edge peak at 7708.5 eV, a value identical to that observed for cobalt phthalocyanine (CoPc), which suggested the presence of a planar Co-N₄ coordination environment [52, 53]. Besides, the Co peak of Co-N₄/NC was located between those of CoO and Co₃O₄, i.e., the Co oxidation state lied between +2 and +3. Furthermore, the Fourier-transformed K^2 -weighted $\chi(k)$ function of EXAFS spectra in R -space was used to quantify coordination numbers and bond lengths. For Co-N₄/NC (Fig. 4b), a prominent peak at 1.47 Å was observed, corresponding to the first

coordination shell of Co-N. This peak was highly similar to that of atomically dispersed Co-N bonds observed for CoPc [52, 53]. The EXAFS fitting results of Co-N₄/NC (Fig. 4c, d) revealed the existence of Co-N bonds (peak at 1.47 Å), with the corresponding coordination number of the central Co atom determined as ~4, which agrees with the planar structure of Co-N₄. (The proposed local atomic structure is illustrated in the inset of Fig. 4.) The wavelet transform was further used to analyze the Co K-edge EXAFS spectra of Co-N₄/NC. Figure 4e shows that for Co-N₄/NC, the maximum intensity was observed at ~3.5 Å⁻¹, which is very close to the value of Co-N in CoPc (~4 Å⁻¹), but quite distinct from that of Co foil (~6.7 Å⁻¹), CoO (4 Å⁻¹ < and/or < 7 Å⁻¹), and Co₃O₄ (5 Å⁻¹ < and/or < 7 Å⁻¹). Therefore, Co-N₄/NC was concluded to contain atomically dispersed planar Co-N₄ motifs.

Similarly, the Fe K-edge XANES spectrum of Fe-N₄/NC was compared to those of three reference materials: Fe foil, Fe₂O₃, and Fe-Pc (Fig. 5a). The spectrum of Fe-N₄/NC featured a pre-edge peak at 7114.8 eV, which was identical to that of iron phthalocyanine (Fe-Pc) with a distinct Fe-N₄ planar structure [54, 55]. Moreover, the peaks of Fe-N₄/NC were located between those of Fe and Fe₂O₃, i.e., the above catalyst contained Fe⁰ and Fe³⁺. Figure 5b presents the Fourier-transformed *K*²-weighted *x(k)* function of the Fe-N₄/NC EXAFS spectrum in *R*-space, revealing a prominent peak at 1.53 Å that is significantly different from that of Fe foil and Fe₂O₃, but is highly similar to that of planar Fe-N coordination in Fe-Pc [54, 56]. The results of Fe-N₄/NC EXAFS spectrum fitting (Fig. 5c, d) revealed a peak of Fe-N at 1.53 Å, with the coordination number of the central Fe atom determined as ~4, showing that the Fe atom is coordinated to four N atoms in the planar structure. The proposed local atomic structure of Fe-N₄/NC is presented in the inset of Fig. 5d. The wavelet transform of Fe-N₄/NC (Fig. 5e) demonstrates only one peak with a maximum at ~4 Å⁻¹, which is relatively close to the value of Fe-Pc (~3.9 Å⁻¹) and completely different from those of Fe foil (~8 Å⁻¹) and Fe₂O₃ (3.5 Å⁻¹ < and/or < 8 Å⁻¹). Therefore, Fe-N₄/NC was concluded to contain atomically distributed planar Fe-N₄ units. The results of detailed X-ray analyses suggest that the ultrasonication-assisted plasma engineering process allows one to preserve the unique planar Co-N₄ and Fe-N₄ coordination motifs within the NC matrix. Even at a low dopant content of < 0.3 wt %, the unique electronic structure and coordination environment of atomic metal-N₄ units could

apparently enhance the ORR/OER activity of carbon-based electrocatalysts.

3.2 ORR/OER Performance

The ORR and OER performances of electrocatalysts were examined using a rotating ring-disk electrode in O₂-saturated 0.1 M KOH. The CV curves of Co-N₄/NC and Fe-N₄/NC featured cathodic peaks at 0.70 and 0.65 V versus RHE, respectively (Fig. S8). Figure 6a, b presents the related linear sweep voltammograms and histograms, showing that the ORR onset potential (*E*_{onset}) and half-wave potential (*E*_{1/2}) of Co-N₄/NC equaled 0.93 and 0.81 V versus RHE, respectively, while the corresponding values of Fe-N₄/NC equaled 0.92 and 0.80 V versus RHE, respectively. Both M-N₄/NCs demonstrated significantly higher ORR activities than pristine NC (*E*_{onset} = 0.81 V and *E*_{1/2} = 0.67 V). These findings prove the importance of single-atom M-N₄ units as efficient ORR active sites despite their very low content of < 0.3 wt %. LSV curves recorded at rotation rates of 400–2000 rpm were used to examine the ORR activity of M-N₄/NCs (Fig. S9). Furthermore, RRDE were simultaneously collected to calculate electron transfer number (*n*) and H₂O₂ yield of Co-N₄/NC, Fe-N₄/NC and 20 wt % Pt/C. As shown in Fig. S9a, both single-atom-doped catalysts show calculated *n* values above 3.6 over the potential range of 0.2–0.8 V, revealing high ORR selectivity and efficient 4e⁻ transfer mechanism. Figure S9b illustrates that the H₂O₂ percentage of Co-N₄/NC was below 29%. Figure 6c compares the ORR Tafel slopes of Fe-N₄/NC, Co-N₄/NC, NC, and 20 wt % Pt/C to further analyze the ORR mechanism. The Tafel slopes of Fe-N₄/NC (65 mV dec⁻¹) and Co-N₄/NC (51 mV dec⁻¹) were lower than that of 20 wt % Pt/C (99 mV dec⁻¹), while NC showed a higher slope of 110 mV dec⁻¹. This result indicated that the ORR kinetics of Co-N₄/NC were superior to those of other catalysts. The electrochemical impedance spectrum of Co-N₄/NC (Fig. 6d) presented the smallest-radius semicircle in the intermediate frequency range, i.e., this catalyst exhibited a lower charge transfer resistance than Fe-N₄/NC and NC. Long-term cycling stability is a crucial indicator of electrocatalyst performance. Cycling did not significantly affect the electrochemical impedance spectrum of Co-N₄/NC (Fig. 6e), although charge transfer resistance increased by ~10% after 100



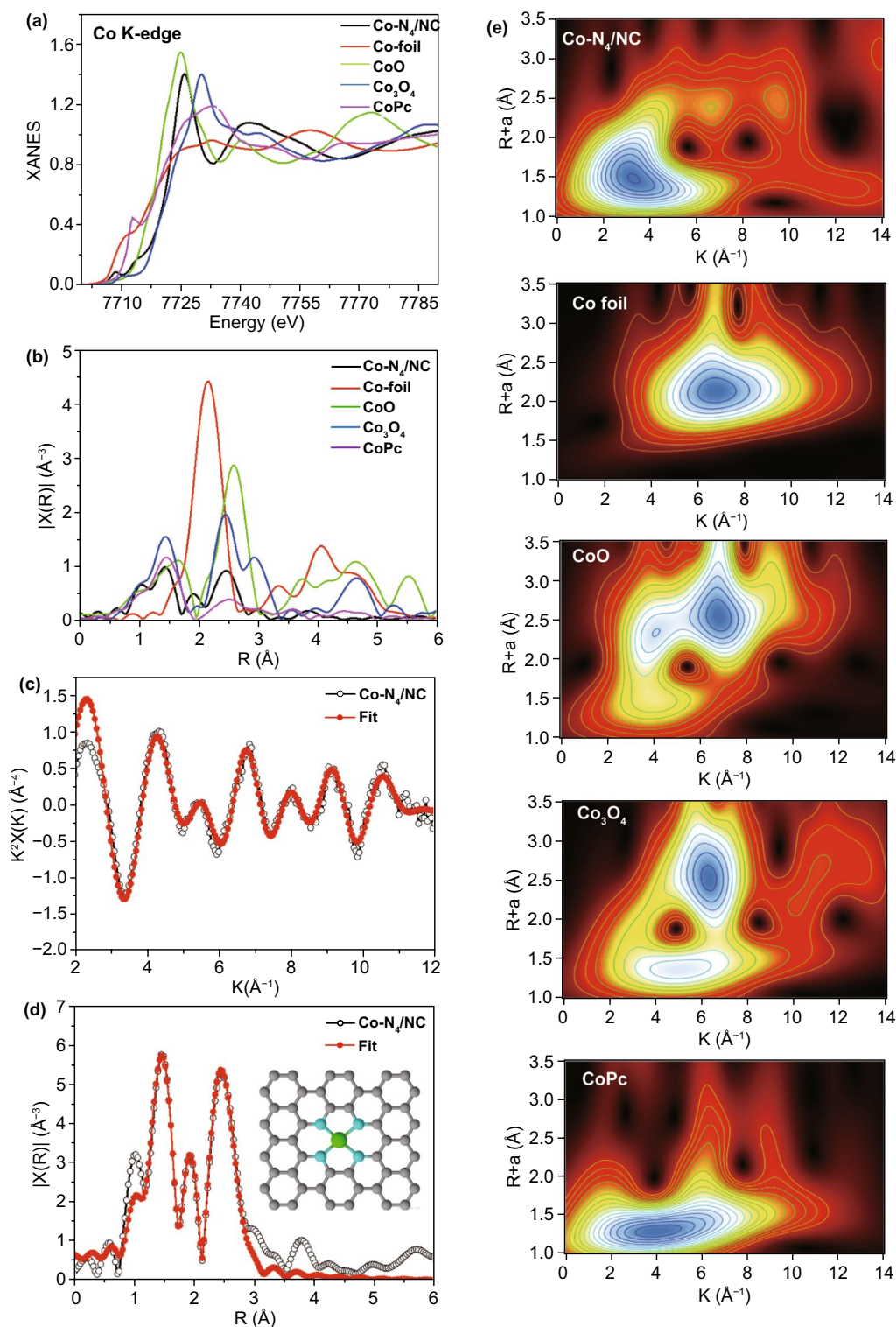


Fig. 4 The local electronic state and chemical environment of Co-N₄/NC. **a** Comparison of Co K-edge XANES spectra of Co foil, CoO, Co₃O₄, CoPc, and Co-N₄/NC. **b** Fourier transform of the EXAFS spectra of Co foil, CoO, Co₃O₄, CoPc, and Co-N₄/NC. **c**, **d** EXAFS analysis of Co-N₄/NC at K and R space. The inset in **d** demonstrates the model derived from the EXAFS results. **e** Wavelet transform of Co K-edge XANES spectra of Co foil, CoO, Co₃O₄, CoPc, and Co-N₄/NC

cycles. Moreover, Co-N₄/NC demonstrated a very weak attenuation (~12 mV) of $E_{1/2}$ after 3000 cycles at a sweep rate of 50 mV s⁻¹ (Fig. 6f). Conversely, commercial Pt/C exhibited a larger reduction of $E_{1/2}$ (16 mV) after an identical durability test. These results confirm that single-atom Co-N₄ active sites are firmly anchored within the N-doped graphitic carbon matrix with superior stability. Furthermore, the ORR stability of Co-N₄/NC is determined by the chronoamperometry measurement at a constant potential of 0.6 V for 30,000 s (Fig. S10a) and the chronopotentiometry response at a constant current density of -4 mA cm⁻² for 12,000 s (Fig. S10b). After the durability test, Co-N₄/NC retains 83.6% of its initial current density in Fig. S10a, while exhibiting a slight increase in overpotential after 12,000 s at a constant current density of -4 mA cm⁻² in Fig. S10b. Overall, the single-atom Co-N₄/NC presents relatively high robustness and stability.

The OER activities of Co-N₄/NC and Fe-N₄/NC were also investigated in 0.1 M KOH electrolyte. Among all, Co-N₄/NC features the lowest onset potential (1.52 V) and overpotential (1.60 V) at 10 mA cm⁻², while Fe-N₄/NC exhibited a similar overpotential of 1.63 V at 10 mA cm⁻² (Fig. 6g). Both M-N₄/NCs showed better intrinsic OER activity than 5 wt % Ru/C (overpotential at 10 mA cm⁻² = 1.67 V), while NC showed the worst OER performance (Fig. S11). As shown in Fig. 6h, the Tafel slopes of Co-N₄/NC, Fe-N₄/NC, and Ru/C equaled 138, 145, and 238 mV dec⁻¹, respectively. Thus, Co-N₄/NC presented both the highest OER activity and the best OER kinetics. The OER stability of Co-N₄/NC was determined by the chronoamperometry measurement at a constant potential of 1.6 V for 5000 s. Figure S12 indicates that Co-N₄/NC shows a large attenuation after 5000 s compared to its initial current density, illustrating that there is a certain instability under the relatively high operating potential. Compared to the relatively high ORR stability Co-N₄/NC at a potential of 0.6 V (Fig. S10), the stability at the higher potential range is much lower. The key aspects of the instability of single-atom metal catalysts are mainly due to (1) single-atom migration into cluster and (2) single-atom metal loss due to detachment [57]. Particularly, atomic metal atoms often drift on pristine carbon surfaces to form aggregate particles due to the relatively weak interactions between carbon and metal when compared to the strong sp^2 binding between carbon atoms [58]. Some possible approaches have been reported, including

stabilizing the single metal atoms on defective graphene [59], carbon vacancies [60], or introduction of foreign atoms such as nitrogen or sulfur into the carbon supports [61]. In particular, the atomic structure of M-N₄ moieties was reported to anchor the single-atom metal site securely onto the carbon support [62–64]. For instance, Zhang et al. reported a stable Co center atoms coordinated with four pyridinic N atoms of the Co-N₄ plane [65]. Based on the XANES spectrum, ultrasonic-plasma-engineered Co-N₄/NC catalyst presents very similar pre-edge peak to that of cobalt phthalocyanine (CoPc), which proves the existence of a planar Co-N₄ coordination. Based on the above literature reviews, this stable Co-N₄ structure could have avoided the migration or detachment of single-atom metal active sites from the support. In contrast, the OER stability of Co-N₄/NC still shows low stability. Although the single-atom cobalt metal atoms are anchored strongly via the M-N₄ carbon support, transitional metal active sites are easily oxidized during the OER process at high operating potential of 1.6 V [66]. Li et al. studied the stability of Co/Fe catalysts by in situ and *operando* X-ray absorption spectroscopy (XAS) to probe the structural and oxidation changes of transitional metal elements under 1.6 V versus RHE. Both Co and Fe showed a clear edge shift toward higher energy, which implied that the metal active sites were further oxidized compared to their original states. Furthermore, Co and Fe remain at its high oxidation state and the reaction was irreversible even the electrode potential was switched back to OCV [67].

The potential difference ΔE ($\Delta E = E_{j=10} - E_{1/2}$) is often used as a measure of bifunctional ORR/OER activity. Figure 6i shows that Co-N₄/NC demonstrated the smallest ΔE of 0.79 V, with a slightly higher value of 0.83 V observed for Fe-N₄/NC. For comparison, a 1:1 (w/w) mixture of commercial Pt/C and Ru/C served as the benchmark bifunctional electrocatalyst and exhibited a ΔE of 0.88 V, which exceeded those of Co-N₄/NC and Fe-N₄/NC. The intrinsic ORR/OER activities of Co-N₄/NC and Fe-N₄/NC seemed to be slightly inferior to those of other recently reported single-atom catalysts. Previous DFT calculations and other reports suggest that high metal loadings and well-dispersed metal atoms in M-N₄ matrices are important for superior ORR/OER activity [68]. In contrast to other methods, ultrasonication-assisted plasma engineering allows the simple formation of a fine dispersion of isolated single-atom M-N₄ sites. However, the main

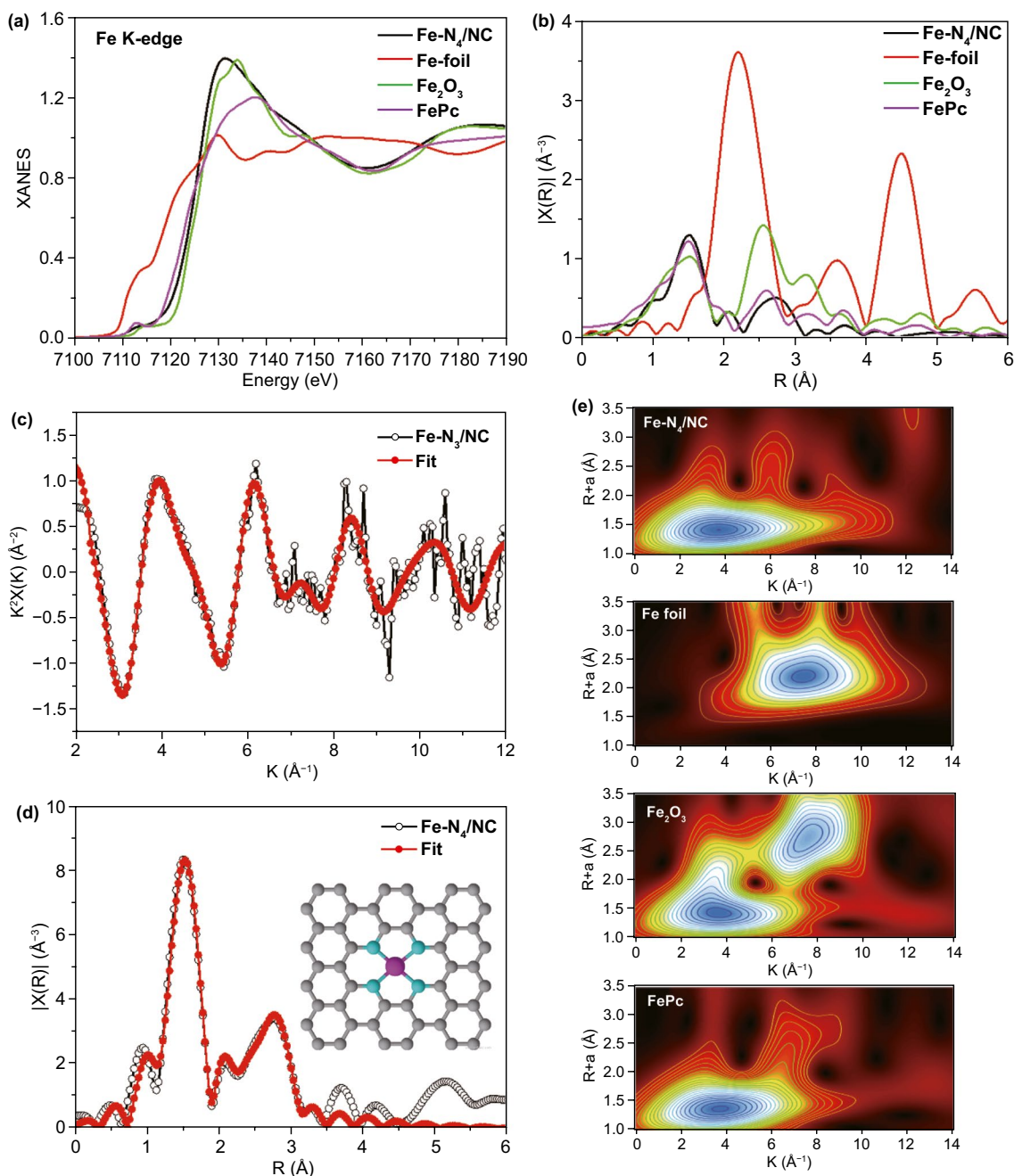


Fig. 5 The local electronic state and chemical environment of Fe-N₄/NC. **a** Comparison of Fe K-edge XANES spectra of Fe foil, Fe₂O₃, FePc, and Fe-N₄/NC. **b** Fourier transform of the EXAFS spectra of Fe foil, Fe₂O₃, FePc, and Fe-N₄/NC. **c, d** EXAFS analysis of Fe-N₄/NC at K and R space, respectively. The inset in **d** demonstrates the model derived from the EXAFS results. **e** Wavelet transform of Fe K-edge XANES spectra of Fe foil, Fe₂O₃, FePc, and Fe-N₄/NC

drawback of this technique is the low solubility of metal phthalocyanines in aniline and other organic solvents. Compared to previously reported single-atom-doped M-N₄ electrocatalysts prepared by high-temperature pyrolysis of MOFs, polymers, or organic compounds, our electrocatalysts presented a small metal loading (<0.3 wt %), but still

exhibited ORR/OER activities comparable to those of isolated Fe or Co electrocatalysts with a similar mass loading (Table S3). Theoretically, the single-atom metal loading can be easily increased if other metal precursors (metal nitrides, metal hydroxides, etc.) with higher solubility in organic solvent are chosen. Also, the energy and frequency

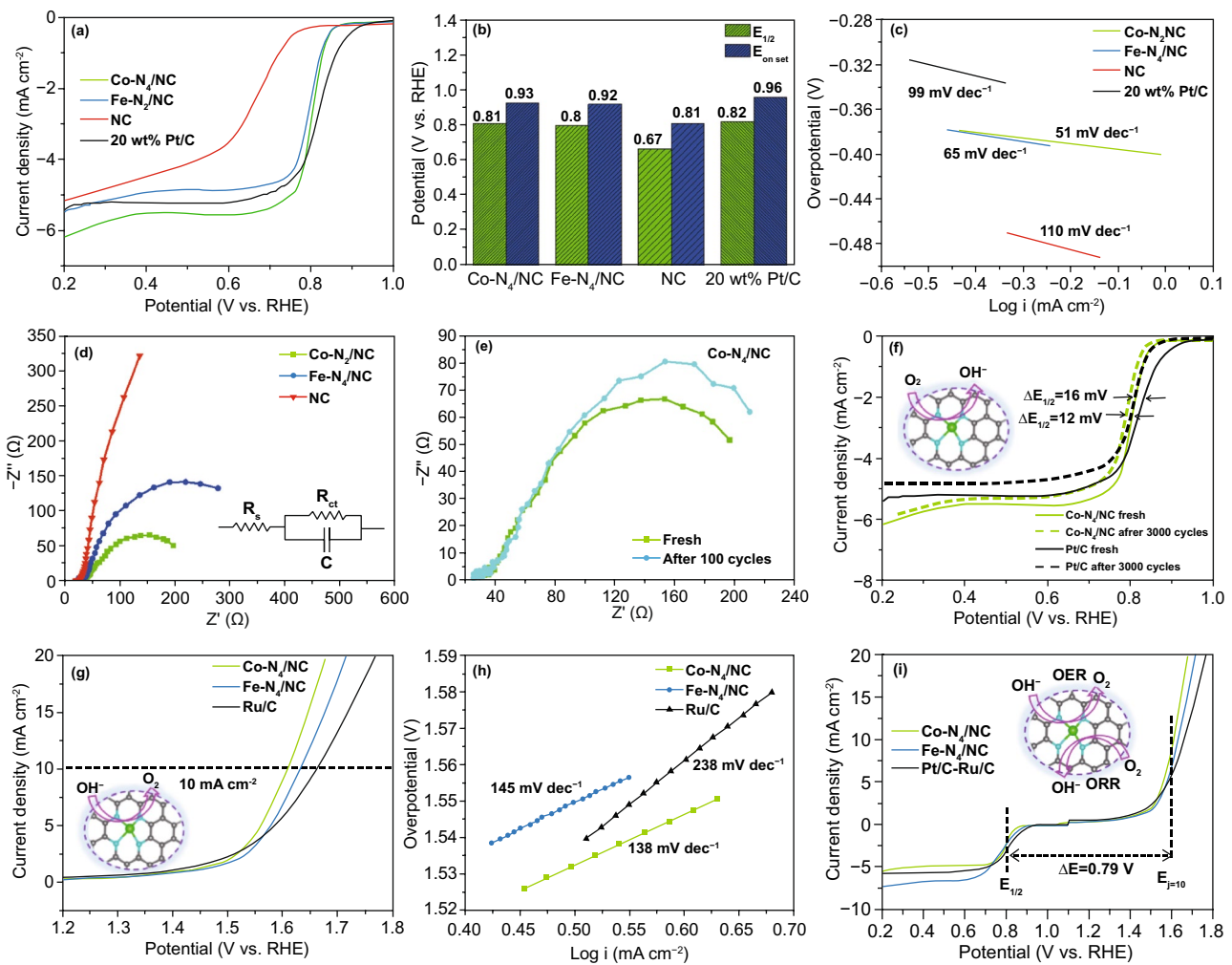


Fig. 6 **a** Linear scan voltammetry (LSV) curves, **b** Half-wave potential and onset potential and, **c** Tafel slopes of Co-N₄/NC, Fe-N₄/NC, NC, and Pt/C for ORR in O₂-saturated 0.1 M KOH solution at 1600 rpm with 5 mV s⁻¹. **d** Electrochemical impedance spectroscopy (EIS) measurements of Co-N₄/NC, Fe-N₄/NC, and NC. **e** EIS of Co-N₄/NC fresh and after 100 cycles. **f** ORR polarization curves of Co-N₄/NC and Pt/C before and after 3000 cycles. **g** LSV polarization curves and **h** Tafel slopes for OER of Co-N₄/NC, Fe-N₄/NC, and Ru/C. **i** LSV polarization curves of different catalysts for ORR/OER in O₂-saturated 0.1 M KOH solution at 1600 rpm with 5 mV s⁻¹

of the ultrasonic device should be designed accordingly to create more cavitation in solution media to ensure single-metal active sites can be atomically dispersed even with higher metal loading. Nevertheless, our approach is believed to be well suited for the scalable synthesis of single-atom metal electrocatalysts.

3.3 DFT Calculations

DFT calculations were performed to obtain deeper insights into the free energy landscape of the ORR and OER. First, we have modeled NC structures with N-doped graphene-based

supercells having low and high defect concentrations according to experimental observation of the various N-doped graphene structures. The relaxed atomic configurations of OER/ORR intermediate adsorbates on NC, Co-N₄/NC, and Fe-N₄/NC are illustrated in Fig. 7a. The ORR/OER reaction steps (I–IV) corresponding to OOH, O, and OH adsorption and H₂O generation are described as follows:

ORR reactions

- (I) O₂(g) + H⁺ + e⁻ → OOH^{*}
- (II) OOH^{*} + H⁺ + e⁻ → O^{*}
- (III) O^{*} + H⁺ + e⁻ → OH^{*}
- (IV) OH^{*} + H⁺ + e⁻ → H₂O(l) + *

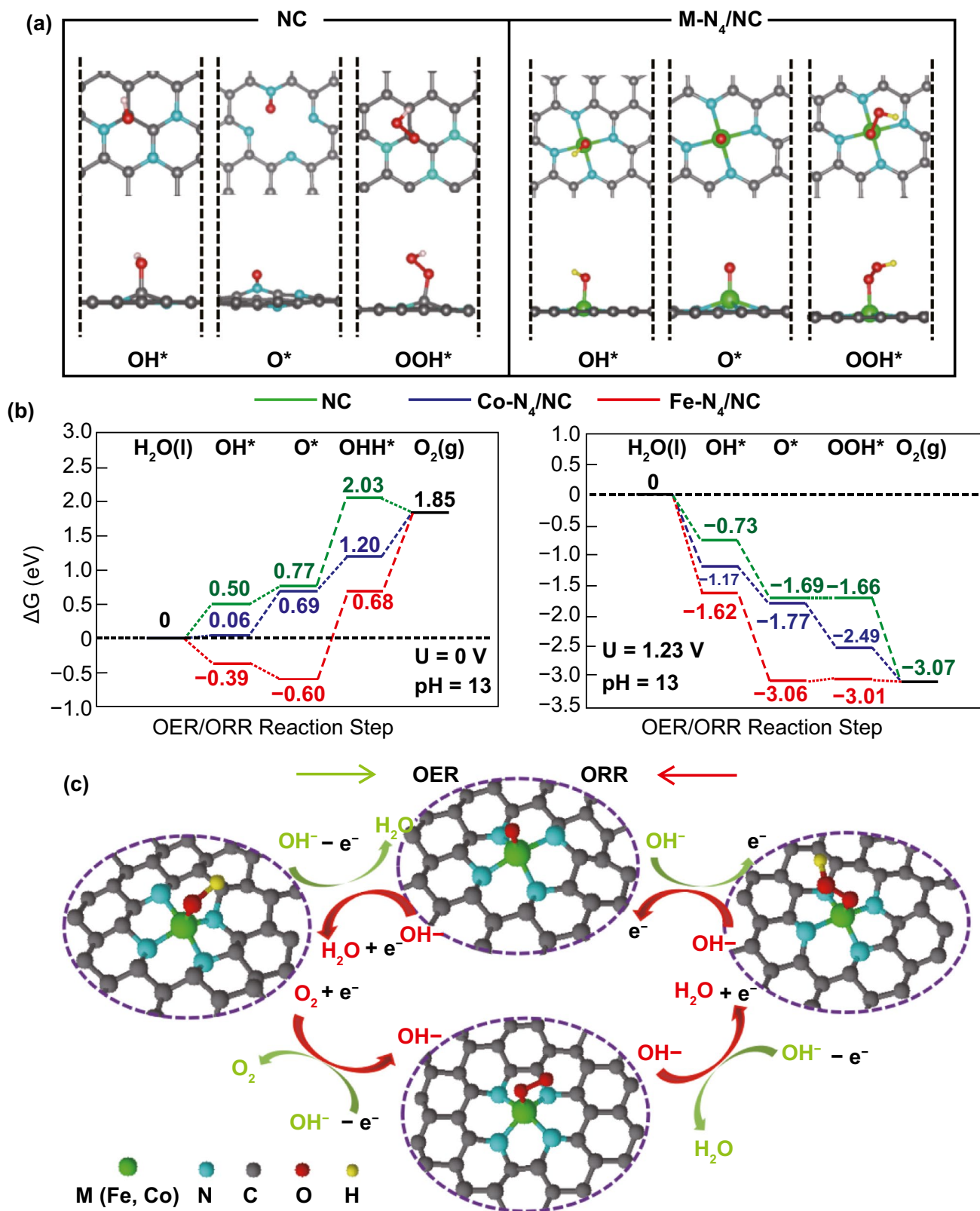
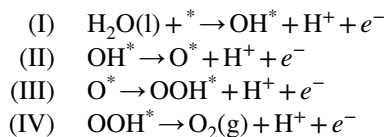


Fig. 7 a Stable adsorption configuration of OER and ORR intermediates on NC and M-N₄/NC. b Calculated free energy landscape for OER and ORR on NC (green), Co-N₄ (blue) and Fe-N₄ (red)—embedded graphene at U=0 V (left) and 1.23 V (right). c Structure of OH*, O*, OOH* adsorbed M-N₄ and the mechanisms in OER/ORR processes. The gray, blue, green, red, and yellow sphere are C, N, M (Fe, Co), O, and H atoms

OER reactions



The calculated OER/ORR free energy of NC was added to compare with those of Co-N₄/NC and Fe-N₄/NC at U = 0 V and U = 1.23 V in Fig. 7b. In the case of NC, several reaction steps of OER and ORR were energetically uphill. For example, a positive energy is required in OER at step III (O* → OOH* + H⁺ + e⁻). In the case of ORR at U = 0 V and 1.23 V, the NC also exhibits a significant energy barrier at the initial step (O₂(g) + H⁺ + e⁻ → OOH*). Compared to that of Co-N₄/NC and Fe-N₄/NC, NC shows much higher energy barriers in both OER and ORR performance, in agreement with its inferior bifunctional catalytic activity in our experimental results. As single-atom-doped M-N₄/NCs have significantly higher OER/ORR activity than NC, one can easily assume that metal-N₄ coordination is the dominant contributor to active sites. Previous DFT calculations also demonstrated that adsorption on single metal (Fe, Co) atoms in M-N₄/NC supercells is much more favorable than that on N or C atoms [69]. Hence, more detailed study of the adsorptions of ORR/OER intermediates (OOH, O, OH) as well as their theoretical overpotentials on these metal sites should be considered. The theoretical overpotential of each catalysts at pH13 is calculated via the following equation:

$$\eta_{\text{OER}}(\text{V}) = \max\{\Delta G_{\text{I}}, \Delta G_{\text{II}}, \Delta G_{\text{III}}, \Delta G_{\text{IV}}\}/e - 0.46 \quad (6)$$

$$\eta_{\text{ORR}}(\text{V}) = 0.46 - \min\{\Delta G_{\text{I}}, \Delta G_{\text{II}}, \Delta G_{\text{III}}, \Delta G_{\text{IV}}\}/e \quad (7)$$

where ΔG_{max} and ΔG_{min} are minimum and maximum Gibbs free energies of the four reaction step of OER.

The $\eta_{\text{OER}}/\eta_{\text{ORR}}$ of Co-N₄ and Fe-N₄ is calculated based on the highest energy barrier at the rate-determining step (RDS). In the case of Co-N₄/NC, the RDS of OER is found to be the conversion of OOH* to O₂ (OOH* → O₂(g) + H⁺ + e⁻), while the last step in ORR (OH* + H⁺ + e⁻ → H₂O(l) + *) requires the highest energy uphill. In case of Fe-N₄/NC, the RDS of OER belongs to step III (O* → OOH* + H⁺ + e⁻), where step IV (OH* + H⁺ + e⁻ → H₂O(l) + *) presents the greatest energy barrier in ORR. Based on their corresponding free energy, the η_{OER} of Co-N₄ and Fe-N₄ calculated from DFT

calculations is 0.19 and 0.82 V, respectively. Meanwhile, the corresponding η_{ORR} of Co-N₄ and Fe-N₄ is reported as 0.40 and 0.85 V. The trends of theoretically OER and ORR overpotential from DFT calculations are well consistent with experimental results, as both overpotentials of Co-N₄/NC obtained from electrochemical are lower than that of Fe-N₄/NC. The theoretical and experimental overpotentials are summarized in Table S5. The detailed pathways of reversible OER/ORR reactions promoted by M-N₄ active sites are summarized in Fig. 7c. Overall, both DFT calculations and electrochemical evaluations confirmed that single-atom Co-N₄/NC is the most promising bifunctional OER/ORR electrocatalyst.

3.4 Evaluation of an In-House-Built ZAB

Rechargeable ZABs are promising energy storage and conversion devices, featuring the advantages of high theoretical specific capacity, intrinsic reliability, and low cost. Therefore, the performance of Co-N₄/NC was further investigated in a practical ZAB, which comprised carbon paper loaded with Co-N₄/NC (1 mg cm⁻²) as the air electrode and polished Zn foil as the anode (Fig. 8a). For comparison, a 1:1 (w/w) mixture of Pt/C-Ru/C was applied with the same catalyst loading. A solution containing 6.0 M KOH and 0.2 M zinc acetate was used as the electrolyte. Figure 8b shows a photograph of two in-house-made ZABs, revealing that the open-circuit voltage of Co-N₄/NC reaches 2.72 V. Figure 8c reveals that at a current density of 20 mA cm⁻², Co-N₄/NC demonstrated a superior specific capacity of 762.8 mAh g⁻¹ (93.0% of the theoretical capacity of 820 mAh g⁻¹), which exceeded that of Pt/C-Ru/C (700.8 mAh g⁻¹). The remarkable specific capacity of Co-N₄/NC at a high current density mainly originated from the excellent conductivity and well-dispersed single-atom Co-N₄ active sites which could significantly enhance electron transfer and ion diffusion. Figure 8d compares the discharge polarization and power density curves of Co-N₄/NC and Pt/C-Ru/C. The discharge voltages of Co-N₄/NC at current densities of 20, 75, and 140 mA cm⁻² were determined to be 1.17, 0.95, and 0.71 V, respectively. At the same time, the benchmark Pt/C-Ru/C electrocatalyst exhibited discharge voltages of 1.19, 0.95, and 0.64 V at 20, 75, and 140 mA cm⁻², respectively. Although Co-N₄/NC showed a slightly inferior discharge voltage at lower current densities of 0–20 mA cm⁻², its

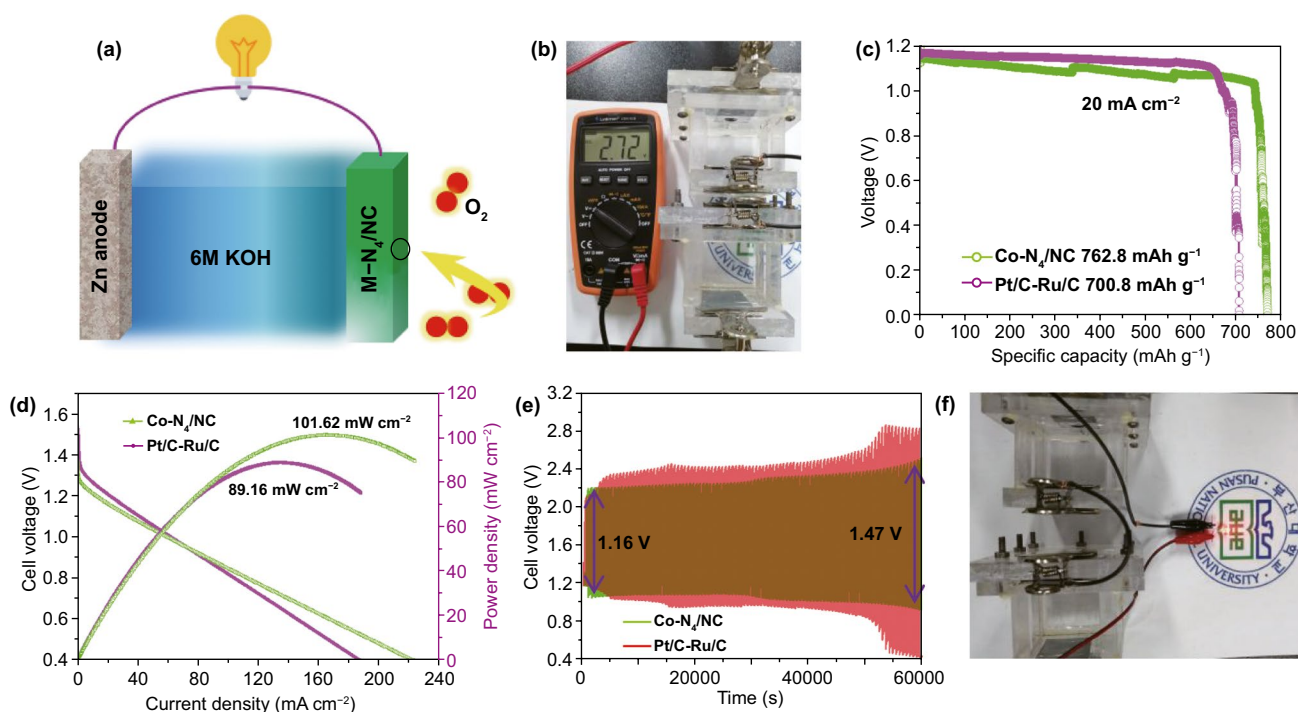


Fig. 8 **a** Schematic of zinc–air battery. **b** Open cell voltage (OCV) of two-connected Zn–air battery. **c** Specific discharging capacities at 20 mA cm^{-2} . **d** Discharging polarization and power density curves based on the Co-N₄/NC and Pt/C-Ru/C catalyst. **e** Cycling test (100 cycles) at a current density of 10 mA cm^{-2} with Co-N₄/NC and Pt/C-Ru/C catalyst. **f** Images of two homemade rechargeable Zn–air batteries in series with a LED

performance significantly improved and exceeded that of Pt/C-Ru/C at current densities above 80 mA cm^{-2} . Besides, the maximum power density of Co-N₄/NC ($101.62 \text{ mW cm}^{-2}$) was significantly higher than that of Pt/C-Ru/C (89.16 mW cm^{-2}). These results indicate that Co-N₄/NC is a better choice than Pt/C-Ru/C for the air electrode of practical ZABs [70]. The galvanostatic cycling performance of the fabricated ZAB was investigated at 10 mA cm^{-2} (Fig. 8e). Although the potential difference for the charge–discharge of Pt/C-Ru/C (0.95 V) was lower during the first 10 cycles, the overpotential rapidly increased to 2.5 V after 100 charge–discharge cycles ($60,000 \text{ s}$) because of the insufficient stability of noble metal nanoparticles on the carbon matrix. In contrast, the potential difference of Co-N₄/NC increased only from 1.16 to 1.47 V under the same condition of 100 cycles (Fig. S13). The open-circuit voltage of the Co-N₄/NC electrode remained at 1.24 V after 100 cycles, which implies that the single-atom Co-N₄ active sites were highly stable and stayed electrochemically active (Figs. S14 and S15). Figure 8f shows that two in-house-made ZABs with Co-N₄/NC as the air electrode could light

up a light-emitting diode when connected in series. Table S4 compares our ZAB to previously reported systems and indicates that the performance of Co-N₄/NC was on par with that of other electrocatalysts.

4 Conclusions

Ultrasonication-assisted plasma engineering was used to incorporate evenly dispersed single-atom M-N₄ (M = Fe, Co) sites into NC, achieving a production rate of $\sim 10 \text{ mg/min}$. The results of physicochemical analysis supported the incorporation of planar M-N₄ structures into the NC matrix, revealing that these structures acted as the major ORR/OER active sites. In an alkaline medium, the single-atom M-N₄/NC (M = Fe, Co) electrocatalysts showed high ORR/OER performance and stability superior to those of benchmark Pt/C and Ru/C catalysts. Specifically, Co-N₄/NC showed a notable potential difference (ΔE) of 0.79 V , outperforming the benchmark Pt/C-Ru/C at the same loading ($\Delta E = 0.88 \text{ V}$). DFT calculations showed that the free

energy landscape of Co-N₄/NC indicated better adsorption–desorption in reversible ORR/OER stages than that of Fe-N₄/NC, which well agreed with the experimental results. In a practical application, Co-N₄/NC demonstrated electrocatalytic activity superior to that of Pt/C-Ru/C, achieving higher power density and durability in a rechargeable ZAB. Thus, herein we describe a promising, versatile, and scalable strategy of synthesizing various types of single-atom metal–carbon catalysts, an important class of frontier catalytic materials widely utilized in metal–air batteries and fuel cells.

Acknowledgements This research was mainly supported by Global Frontier Program through the Global Frontier Hybrid Interface materials (GFHIM) of the National Research Foundation of Korea (NRF) funded by the ministry of science, ICT and Future Planning (2013M3A6B1078874), and co-supported by Busan Innovation Institute of Industry, Science & Technology Planning (BISTEP). MJ and HC acknowledge the financial support of Federal Ministry of Education and Research (BMBF) under the “Make Our Planet Great Again - German Research Initiative” (MOPGA-GRI), 57429784, implemented by the German Academic Exchange Service Deutscher Akademischer Austauschdienst (DAAD). Also, the authors want to thank Dr. Juchul Park for his valuable advice in HR-TEM.

Open Access This article is licensed under a Creative Commons Attribution 4.0 International License, which permits use, sharing, adaptation, distribution and reproduction in any medium or format, as long as you give appropriate credit to the original author(s) and the source, provide a link to the Creative Commons licence, and indicate if changes were made. The images or other third party material in this article are included in the article’s Creative Commons licence, unless indicated otherwise in a credit line to the material. If material is not included in the article’s Creative Commons licence and your intended use is not permitted by statutory regulation or exceeds the permitted use, you will need to obtain permission directly from the copyright holder. To view a copy of this licence, visit <http://creativecommons.org/licenses/by/4.0/>.

Supplementary Information The online version contains supplementary material available at <https://doi.org/10.1007/s40820-020-00581-4>

References

1. J.X. Han, X.Y. Meng, L. Lu, J.J. Bian, Z.P. Li et al., Single-atom Fe-N_x-C as an efficient electrocatalyst for zinc-air batteries. *Adv. Funct. Mater.* **29**, 1808872 (2019). <https://doi.org/10.1002/adfm.201808872>
2. Q.Q. Zhang, J.Q. Guan, Single-atom catalysts for electrocatalytic applications. *Adv. Funct. Mater.* **30**, 2000768 (2020). <https://doi.org/10.1002/adfm.202000768>
3. X.J. Zheng, J. Wu, X.C. Cao, J. Abbott, C. Jin et al., N-, P-, and S-doped graphene-like carbon catalysts derived from onium salts with enhanced oxygen chemisorption for Zn-air battery cathodes. *Appl. Catal. B: Environ.* **241**, 442–451 (2019). <https://doi.org/10.1016/j.apcatb.2018.09.054>
4. Y. Tong, P.Z. Chen, T.P. Zhou, K. Xu, W.S. Chu et al., A bifunctional hybrid electrocatalyst for oxygen reduction and evolution: cobalt oxide nanoparticles strongly coupled to B,N-decorated graphene. *Angew. Chem. Int. Ed.* **56**(25), 7121–7125 (2017). <https://doi.org/10.1002/anie.201702430>
5. N.N. Xu, J.A. Wilson, Y.D. Wang, T.S. Su, Y.N. Wei et al., Flexible self-supported bi-metal electrode as a highly stable carbon- and binder-free cathode for large-scale solid-state zinc-air batteries. *Appl. Catal. B: Environ.* **272**(5), 118953 (2020). <https://doi.org/10.1016/j.apcatb.2020.118953>
6. C. Guan, A. Sumboja, H.J. Wu, W.N. Ren, X.M. Liu et al., Hollow Co₃O₄ nanosphere embedded in carbon arrays for stable and flexible solid-state zinc-air batteries. *Adv. Mater.* **29**, 1704117 (2017). <https://doi.org/10.1002/adma.201704117>
7. Y.F. Yuan, K. Amine, J. Lu, R. Shahbazian-Yassar, Understanding materials challenges for rechargeable ion batteries with in situ transmission electron microscopy. *Nat. Commun.* **8**, 1–14 (2017). <https://doi.org/10.1038/ncomms15806>
8. S.H. Su, J.W. Miao, L.P. Zhang, J.J. Gao, H.M. Wang et al., An earth-abundant catalyst-based seawater photoelectrolysis system with 17.9% solar-to-hydrogen efficiency. *Adv. Mater.* **30**, 1707261 (2018). <https://doi.org/10.1002/adma.201707261>
9. L.Q. Li, J. Yang, H.B. Yang, L.P. Zhang, J.J. Shao et al., Anchoring Mn₃O₄ nanoparticles on oxygen functionalized carbon nanotubes as bifunctional catalyst for rechargeable zinc-air battery. *ACS Appl. Energy Mater.* **1**(3), 963–969 (2018). <https://doi.org/10.1021/acsaem.8b00009>
10. Z.H. Wang, H.H. Jin, T. Meng, K. Liao, W.Q. Meng et al., Fe, Cu-coordinated ZIF-derived carbon framework for efficient oxygen reduction reaction and zinc-air batteries. *Adv. Funct. Mater.* **28**(39), 1802596 (2018). <https://doi.org/10.1002/adfm.201802596>
11. H.G. Zhang, S.H. Wang, M.Y. Wang, Z.X. Feng, S. Karakalos et al., Single atomic iron catalysts for oxygen reduction in acidic media: particle size control and thermal activation. *J. Am. Chem. Soc.* **139**(40), 14143–14149 (2017). <https://doi.org/10.1021/jacs.7b06514>
12. C.Z. Zhu, Q.R. Shi, B.Z. Xu, S.F. Fu, G. Wan et al., Hierarchically porous M–N–C (M = Co and Fe) single-atom electrocatalysts with robust MN_x active moieties enable enhanced ORR performance. *Adv. Energy Mater.* **8**(29), 1801956 (2018). <https://doi.org/10.1002/aenm.201801956>
13. S.S. Zheng, X.R. Li, B.Y. Yan, Q. Hu, Y.X. Xu et al., Transition-metal (Fe Co, Ni) based metal-organic frameworks for electrochemical energy storage. *Adv. Energy Mater.* **7**(18), 1602733 (2017). <https://doi.org/10.1002/aenm.201602733>
14. M.F. Wang, T. Qian, J.Q. Zhou, C.L. Yan, An efficient bifunctional electrocatalyst for a zinc-air battery derived from Fe/N/C and bimetallic metal-organic framework composites. *ACS Appl. Mater. Interfaces* **9**(6), 5213–5221 (2017). <https://doi.org/10.1021/acsaami.6b12197>



15. X.P. Han, X.F. Ling, D.S. Yu, D.Y. Xie, L.L. Li et al., Atomically dispersed binary Co–Ni sites in nitrogen-doped hollow carbon nanocubes for reversible oxygen reduction and evolution. *Adv. Mater.* **31**, 1905622 (2019). <https://doi.org/10.1002/adma.201905622>
16. X.P. Han, X.F. Ling, Y. Wang, T.Y. Ma, C. Zhong et al., Spatial isolation of zeolitic imidazole frameworks-derived cobalt catalysts: from nanoparticle, atomic cluster to single atom. *Angew. Chem. Int. Ed.* **58**, 5359–5364 (2019). <https://doi.org/10.1002/anie.2019011>
17. W.J. Zang, A. Sumboja, Y.Y. Ma, H. Zhang, Y. Wu et al., Single Co atoms anchored in porous N-doped carbon for efficient zinc-air battery cathodes. *ACS Catal.* **8**, 8961–8969 (2018). <https://doi.org/10.1021/acscatal.8b02556>
18. M.F. Craciun, S. Rogge, A.F. Morpurgo, Correlation between molecular orbitals and doping dependence of the electrical conductivity in electron-doped metal-phthalocyanine compounds. *J. Am. Chem. Soc.* **127**(35), 12210–12211 (2005). <https://doi.org/10.1021/ja054468j>
19. M.F. Craciun, S. Rogge, M.J.L. den Boer, S. Margadonna, K. Prassides et al., Electronic transport through electron-doped metal phthalocyanine materials. *Adv. Mater.* **18**(3), 320–324 (2006). <https://doi.org/10.1002/adma.200501268>
20. W.Z. Shen, W.B. Fan, Nitrogen-containing porous carbons: synthesis and application. *J. Mater. Chem. A* **1**(4), 999–1013 (2013). <https://doi.org/10.1039/C2TA00028H>
21. L. Yang, X.F. Zeng, W.C. Wang, D.P. Cao, Recent progress in MOF-derived, heteroatom-doped porous carbons as highly efficient electrocatalysts for oxygen reduction reaction in fuel cells. *Adv. Funct. Mater.* **28**(7), 1704537 (2018). <https://doi.org/10.1002/adfm.201704537>
22. C.Z. Zhu, Q.R. Shi, B.Z. Xu, S.F. Fu, G. Wan et al., Hierarchically porous M–N–C (M = Co and Fe) single-atom electrocatalysts with robust MN_x active moieties enable enhanced ORR performance. *Adv. Energy Mater.* **8**, 1801956 (2018). <https://doi.org/10.1002/aenm.201801956>
23. X.P. Han, W. Zhang, X.Y. Ma, C. Zhong, N.Q. Zhao et al., Identifying the activation of bimetallic sites in NiCo₂S₄@g-C₃N₄-CNT hybrid electrocatalysts for synergistic oxygen reduction and evolution. *Adv. Mater.* **31**, 1808281 (2019). <https://doi.org/10.1002/adma.201808281>
24. J. Zhao, Y. He, Z.L. Chen, X.R. Zheng, X.P. Han et al., Engineering the surface metal active sites of nickel cobalt oxide nanoplates toward enhanced oxygen electrocatalysis for Zn-air battery. *ACS Appl. Mater. Interfaces* **11**, 4915–4921 (2018). <https://doi.org/10.1021/acsami.8b16473>
25. Y.Q. Wang, L. Tao, Z.H. Xiao, R. Chen, Z.Q. Jiang et al., 3D carbon electrocatalysts in situ constructed by defect-rich nanosheets and polyhedrons from NaCl-sealed zeolitic imidazolate frameworks. *Adv. Funct. Mater.* **28**(11), 1705356 (2018). <https://doi.org/10.1002/adfm.201705356>
26. T.T. Wang, Z.K. Kou, S.C. Mu, J.P. Liu, D.P. He et al., 2D dual-metal zeolitic-imidazolate-framework-(ZIF)-derived bifunctional air electrodes with ultrahigh electrochemical properties for rechargeable zinc-air batteries. *Adv. Funct. Mater.* **28**(5), 1705048 (2018). <https://doi.org/10.1002/adfm.201705048>
27. E. Lam, J.H.T. Luong, Carbon materials as catalyst supports and catalysts in the transformation of biomass to fuels and chemicals. *ACS Catal.* **4**(10), 3393–3410 (2014). <https://doi.org/10.1021/cs5008393>
28. M.M. Liu, L.L. Wang, K.N. Zhao, S.S. Shi, Q.S. Shao et al., Atomically dispersed metal catalysts for the oxygen reduction reaction: synthesis, characterization, reaction mechanisms and electrochemical energy applications. *Energy Environ. Sci.* **12**, 2890–2923 (2019). <https://doi.org/10.1039/C9EE01722D>
29. J. Kang, O.L. Li, N. Saito, Synthesis of structure-controlled carbon nano spheres by solution plasma process. *Carbon* **60**, 292–298 (2013). <https://doi.org/10.1016/j.carbon.2013.04.040>
30. G. Panomsuwan, S. Chiba, Y. Kaneko, N. Saito, T. Ishizaki, In situ solution plasma synthesis of nitrogen-doped carbon nanoparticles as metal-free electrocatalysts for the oxygen reduction reaction. *J. Mater. Chem. A* **2**, 18677–18686 (2014). <https://doi.org/10.1039/C4TA03010A>
31. K. Chen, S.H. Kim, R. Rajendiran, K. Prabakar, G.Z. Li et al., Enhancing ORR/OER active sites through lattice distortion of Fe-enriched FeNi₃ intermetallic nanoparticles doped N-doped carbon for high-performance rechargeable Zn-air battery. *J. Colloid Interface Sci.* **582**(15), 977–990 (2021). <https://doi.org/10.1016/j.jcis.2020.08.101>
32. S. Lee, U. Heo, M.A. Mratescu, T. Ueno, N. Saito, Solution plasma synthesis of a boron–carbon–nitrogen catalyst with a controllable bond structure. *Phys. Chem. Chem. Phys.* **19**, 15264–15272 (2017). <https://doi.org/10.1039/C6CP06063C>
33. O.L. Li, H. Lee, T. Ishizaki, Recent progress in solution plasma-synthesized-carbon-supported catalysts for energy conversion systems. *Jpn. J. Appl. Phys.* **57**, 0102A2 (2018). <https://doi.org/10.7567/JJAP.57.0102A2>
34. T. Morishita, T. Ueno, G. Panomsuwan, J. Hieda, A. Yoshida et al., Fastest formation routes of nanocarbons in solution plasma processes. *Sci. Rep.* **6**, 36880–36892 (2016). <https://doi.org/10.1038/srep36880>
35. P. Mohanty, R. Mahapatra, P. Padhi, C.H.V.V. Ramana, D.K. Mishra, Ultrasonic cavitation: An approach to synthesize uniformly dispersed metal matrix nanocomposites—A review. *Nano-Struct. Nano-Objects* **23**, 100475 (2020). <https://doi.org/10.1016/j.nanoso.2020.100475>
36. M.J. Chen, Y.H. He, J.S. Spendelow, G. Wu, Atomically dispersed metal catalysts for oxygen reduction. *ACS Energy Lett.* **4**(7), 1619–1633 (2019). <https://doi.org/10.1021/acsenenergylt.9b00804>
37. Y. Wang, H. Yuan, Y.F. Li, Z.F. Chen, Two-dimensional iron-phthalocyanine (Fe–Pc) monolayer as a promising single-atom-catalyst for oxygen reduction reaction: a computational study. *Nanoscale* **7**, 11633–11641 (2015). <https://doi.org/10.1039/C5NR00302D>
38. Y. Peng, B.Z. Lu, S.W. Chen, Carbon-supported single atom catalysts for electrochemical energy conversion and storage. *Adv. Mater.* **30**, 1801995 (2018). <https://doi.org/10.1002/adma.201801995>

39. H.L. Fei, J.C. Dong, Y.X. Feng, C.S. Allen, C.Z. Wan et al., General synthesis and definitive structural identification of MN_4C_4 single-atom catalysts with tunable electrocatalytic activities. *Nat. Catal.* **1**, 63–72 (2018). <https://doi.org/10.1038/s41929-017-0008-y>
40. F. Ghani, J. Kristen, H. Riegler, Solubility properties of unsubstituted metal phthalocyanines in different types of solvents. *J. Chem. Eng. Data* **57**(2), 439–449 (2012). <https://doi.org/10.1021/je2010215>
41. B. Ravel, M. Newville, A THENA, ARTEMIS, HEPHAESTUS: data analysis for X-ray absorption spectroscopy using IFEFFIT. *J. Synchrotron Radiat.* **12**, 537–541 (2005). <https://doi.org/10.1107/S0909049505012719>
42. G. Kresse, J. Furthmuller, Efficiency of ab-initio total energy calculations for metals and semiconductors using a plane-wave bases set. *Comput. Mater. Sci.* **6**, 15–50 (1996). [https://doi.org/10.1016/0927-0256\(96\)00008-0](https://doi.org/10.1016/0927-0256(96)00008-0)
43. G. Kresse, D. Joubert, From ultrasoft pseudopotentials to the projector augmented-wave method. *Phys. Rev. B* **59**, 1758–1775 (1999). <https://doi.org/10.1103/PhysRevB.59.1758>
44. J.P. Perdew, J.A. Chevary, S.H. Vosko, K.A. Jackson, M.R. Pederson et al., Atoms, molecules, solids, and surfaces: applications of the generalized gradient approximation for exchange and correlation. *Phys. Rev. B* **46**, 6671–6687 (1992). <https://doi.org/10.1103/PhysRevB.46.6671>
45. J.P. Perdew, K. Burke, M. Ernzerhof, Generalized gradient approximation made simple. *Phys. Rev. Lett.* **77**, 3865–3868 (1996). <https://doi.org/10.1103/PhysRevLett.77.3865>
46. M. Methfessel, A.T. Paxton, High-precision sampling for brillouin-zone integration in metals. *Phys. Rev. B* **40**, 3616–3621 (1989). <https://doi.org/10.1103/PhysRevB.40.3616>
47. P.T. Liu, D.Q. Gao, W. Xiao, L. Ma, K. Sun et al., Self powered water-splitting devices by core-shell NiFe@N-graphite based Zn-air batteries. *Adv. Funct. Mater.* **28**(14), 1706928 (2018). <https://doi.org/10.1002/adfm.201706928>
48. Y.L. Zhang, Z.J. Mu, C. Yang, Z.K. Xu, S. Zhang et al., Rational design of MXene/1T-2H MoS₂-C nanohybrids for high-performance lithium-sulfur batteries. *Adv. Funct. Mater.* **28**(38), 1707578 (2018). <https://doi.org/10.1002/adfm.201707578>
49. X.Y. Qiu, X.H. Yan, H. Pang, J.C. Wang, D.M. Sun et al., Isolated Fe single atomic sites anchored on highly steady hollow graphene nanospheres as an efficient electrocatalyst for the oxygen reduction reaction. *Adv. Sci.* **6**(2), 1801103 (2019). <https://doi.org/10.1002/advs.201801103>
50. M. Li, S.J. Wu, X.Y. Yang, J. Hu, L. Peng et al., Highly efficient single atom cobalt catalyst for selective oxidation of alcohols. *Appl. Catal. A Gen.* **543**(5), 61–66 (2017). <https://doi.org/10.1016/j.apcata.2017.06.018>
51. Y. Pan, S.J. Liu, K. Sun, X. Chen, B. Wang et al., A bimetallic Zn/Fe polyphthalocyanine-derived single-atom Fe–N₄ catalytic site: a superior trifunctional catalyst for overall water splitting and Zn-air batteries. *Angew. Chem. Int. Ed.* **57**(28), 8614–8618 (2018). <https://doi.org/10.1002/anie.201804349>
52. L. Yang, L. Shi, D. Wang, Y.L. Lv, D.P. Cao, Single-atom cobalt electrocatalysts for foldable solid-state Zn-air battery. *Nano Energy* **50**, 691–698 (2018). <https://doi.org/10.1016/j.nanoen.2018.06.023>
53. K. Kim, T. Kang, M. Kim, J. Kim, Three-dimensional entangled and twisted structures of nitrogen doped poly-(1,4-diethynylbenzene) chain combined with cobalt single atom as a highly efficient bifunctional electrocatalyst. *Appl. Catal. B: Environ.* **275**, 119107 (2020). <https://doi.org/10.1016/j.apcatb.2020.119107>
54. K. Yuan, D. Lützenkirchen-Hecht, L.B. Li, L. Shuai, Y.Z. Li et al., Boosting oxygen reduction of single iron active sites via geometric and electronic engineering: nitrogen and phosphorus dual coordination. *J. Am. Chem. Soc.* **142**(5), 2404–2412 (2020). <https://doi.org/10.1021/jacs.9b11852>
55. K. Yuan, S. Sfaelou, M. Qiu, D. Lützenkirchen-Hecht, X.D. Zhuang et al., Synergetic contribution of boron and Fe–N_x species in porous carbons toward efficient electrocatalysts for oxygen reduction reaction. *ACS Energy Lett.* **3**(1), 252–260 (2018). <https://doi.org/10.1021/acseenergylett.7b01188>
56. C.C. Hou, L.L. Zou, L.M. Sun, K.X. Zhang, Z. Liu et al., Single-atom iron catalysts on overhang-eave carbon cages for high-performance oxygen reduction reaction. *Angew. Chem. Int. Ed.* **132**, 7454–7459 (2020). <https://doi.org/10.1002/ange.202002665>
57. N.C. Cheng, L. Zhang, K. Doyle-Davis, X.L. Sun, Single-atom catalysts: from design to application. *Electrochem. Energy Rev.* **2**, 539–573 (2019). <https://doi.org/10.1007/s41918-019-00050-6>
58. N.C. Cheng, S. Stambula, D. Wang, M.N. Banis, J. Liu et al., Platinum single-atom and cluster catalysis of the hydrogen evolution reaction. *Nat. Commun.* **7**, 13638 (2016). <https://doi.org/10.1038/ncomms13638>
59. H.J. Qiu, Y. Ito, W.T. Cong, Y.W. Tan, P. Liu et al., Nanoporous graphene with single-atom nickel dopants: an efficient and stable catalyst for electrochemical hydrogen production. *Angew. Chem. Int. Ed.* **54**, 14031–14035 (2015). <https://doi.org/10.1002/anie.201507381>
60. C. Gao, S.M. Chen, Y. Wang, J.W. Wang, X.S. Zheng et al., Heterogeneous single-atom catalyst for visible-light-driven high-turnover CO₂ reduction: the role of electron transfer. *Adv. Mater.* **30**, 1704624 (2018). <https://doi.org/10.1002/adma.201704624>
61. H.L. Fei, J.C. Dong, M.J. Arellano-Jimenez, G.L. Ye, N.D. Kim et al., Atomic cobalt on nitrogen-doped graphene for hydrogen generation. *Nat. Commun.* **6**, 8668 (2015). <https://doi.org/10.1038/ncomms9668>
62. W.G. Liu, L.L. Zhang, W.S. Yan, X.Y. Liu, X.F. Yang et al., Single-atom dispersed Co–N–C catalyst: structure identification and performance for hydrogenative coupling of nitroarenes. *Chem. Sci.* **7**, 5758–5764 (2016). <https://doi.org/10.1039/C6SC02105K>
63. A.J. Han, W.X. Chen, S.L. Zhang, M.L. Zhang, Y.H. Han et al., A polymer encapsulation strategy to synthesize porous nitrogen-doped carbon-nanosphere-supported metal isolated-single-atomic-site catalysts. *Adv. Mater.* **30**, 1706508 (2018). <https://doi.org/10.1002/adma.201706508>



64. Y. Cheng, S.Y. Zhao, B. Johannessen, J.P. Veder, M. Saunders et al., Atomically dispersed transition metals on carbon nanotubes with ultrahigh loading for selective electrochemical carbon dioxide reduction. *Adv. Mater.* **30**, 1706287 (2018). <https://doi.org/10.1002/adma.201706287>
65. X.L. Zhang, Z.S. Lu, Z.X. Yang, Single non-noble-metal cobalt atom stabilized by pyridinic vacancy graphene: an efficient catalyst for CO oxidation. *J. Mol. Catal. A: Chem.* **417**, 28–35 (2016). <https://doi.org/10.1016/j.molcata.2016.03.008>
66. W.H. Lee, W.-J. Ko, J.-Y. Kim, B.K. Min, Y.J. Hwang et al., Single-atom catalysts for the oxygen evolution reaction: recent developments and future perspectives. *Chem. Comm.* **56**, 12687 (2020). <https://doi.org/10.1039/D0CC04752J>
67. P. Li, M. Wang, X. Duan, L. Zheng, X. Chen et al., Boosting oxygen evolution of single-atomic ruthenium through electronic coupling with cobalt-iron layered double hydroxides. *Nat. Comm.* **10**, 1711 (2019). <https://doi.org/10.1038/s41467-019-09666-0>
68. J.B. Wu, H. Zhou, Q. Li, M. Chen, J. Wan et al., Densely populated isolated single Co–N site for efficient oxygen electrocatalysis. *Adv. Energy Mater.* **9**, 1900149 (2019). <https://doi.org/10.1002/aenm.201900149>
69. S. Kattel, G.F. Wang, Reaction pathway for oxygen reduction on FeN₄ embedded graphene. *J. Phys. Chem. Lett.* **5**(3), 452–456 (2014). <https://doi.org/10.1021/jz402717r>
70. F.L. Meng, H.X. Zhong, D. Bao, J.M. Yan, X.B. Zhang, In situ coupling of strung Co₄N and intertwined N–C fibers toward free-standing bifunctional cathode for robust, efficient, and flexible Zn-air batteries. *J. Am. Chem. Soc.* **138**(32), 10226–10231 (2016). <https://doi.org/10.1021/jacs.6b05046>